AUTHOR(S):

TITLE:

YEAR:

Publisher citation:

OpenAIR citation:

Accepted Manuscript

Title: Unique corrosion resistance of ultrahigh pressure
Mg-25Al binary alloys

Authors: Jiawen Feng, Hanning Li, Kunkun Deng, Carlos
Fernandez, Qingrui Zhang, Qiuming Peng
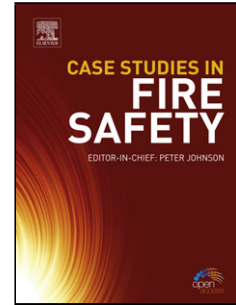
Please cite this article as: Feng J, Li H, Deng K, Fernandez C, Zhang Q, Peng Q, Unique
corrosion resistance of ultrahigh pressure Mg-25Al binary alloys, *Corrosion Science*
(2018), https://doi.org/10.1016/j.corsci.2018.08.013

This is a PDF file of an unedited manuscript that has been accepted for publication.
As a service to our customers we are providing this early version of the manuscript.
The manuscript will undergo copyediting, typesetting, and review of the resulting proof
before it is published in its final form. Please note that during the production process
errors may be discovered which could affect the content, and all legal disclaimers that
apply to the journal pertain.

Unique corrosion resistance of ultrahigh pressure Mg-25Al binary alloys

Jiawen Feng[1], Hanning Li[1], Kunkun Deng[2], Carlos Fernandez[3], Qingrui Zhang[4], Qiuming Peng[,1],*

[1]State Key Laboratory of Metastable Materials Science and Technology, Yanshan University, Qinhuangdao, 066004, PR. China.

[2]College of Materials Science and Engineering, Taiyuan University of Technology, Taiyuan 030024, PR China.

[3]School of Pharmacy and Life Sciences, Robert Gordon University, Aberdeen, AB107GJ, UK

[4]Hebei Key Laboratory of Applied Chemistry, School of Environmental and Chemical Engineering, Yanshan University, Qinhuangdao 066004, P.R. China,

* Corresponding author. Tel.: +86-335-8057439; fax: +86-335-8074545

Email address: pengqiuming@ysu.edu.cn

Highlight

- Ultrahigh pressure solid solution with aging is a way to enhance corrosion
- Obvious age-hardening response is detected in Mg-Al binary system
- An intrinsic Al-rich layer accounts for high anti-corrosion of Mg-Al alloys
- Nanosized beta phase containing high-index planes offers high activity.

Abstract

Differing from as-cast and solid-solution alloys with coarse eutectic phases ($Mg_{17}Al_{12}$), a

single-phase structure is attained in Mg-25wt.%Al alloy after ultrahigh-pressure solid-solution

(USS, 800 ^{o}C, 4GPa). This USSed Mg-25wt.%Al sample exhibits a prominent age-hardening

response due to the nano-scaled $Mg_{17}Al_{12}$ particles. Three testing methods confirm that

USS-aged Mg-25wt.%Al alloy shows good corrosion resistance, which overwhelms the

majority of Mg-based alloys reported so far, near to high purity Mg. The main reason is

attributed to the formation of Al-rich oxide layer, wherein residual stress and pitting corrosion

are eliminated. It provides a new avenue for developing corrosion resistant Mg alloys.

1. Introduction

In relation to environmental protection and sustainable development, Mg alloys have attracted much attention for applications in automotive, aerospace, biomedical and electronic goods sectors, due to their high specific strength, low density and good castability [1]. However, the poor corrosion resistant performance limits their service applications. It is desirable to improve their corrosion resistant performance for widespread applications of Mg alloys, especially for medical Mg-based implants. Although high purity Mg has good corrosion resistant properties due to a low concentration of impurity [2], both poor strength and weak deformability limit its wider applications. In this regard, high corrosion resistant Mg alloys are more essential for engineering applications. Indeed, this issue has been intensively investigated in the past decades, and is well summarized in recent reviews [3-7]. Some methods, such as alloying, surface treatments and coating technology, have been implemented to improve their corrosion resistance. Differing from alloying, surface treatment and coatings, such as polymers [8], ceramics [9], inorganic compounds [10] *etc*, could improve temporary corrosion resistance by separating medium and electrodes. However, as soon as coating is destroyed or gone, this protection role will eliminate, and even accelerate corrosion [10, 11]. Undoubtedly, the corrosion properties of intrinsic matrix eventually determine long-term corrosion properties of Mg alloys. Improving the corrosion resistance of Mg matrix becomes an inevitable issue. Unfortunately, none of commercial Mg alloys reported so far [5] have adequate corrosion resistance in NaCl-containing solutions with high purity Mg.

Theoretically, the major reason for poor corrosion resistance of Mg alloys stems from the loose oxide film with a low Pilling-Bedworth ratio (~0.8) [12], wherein some cracks are prone

to form in the interface between MgO/Mg(OH)$_2$ and Mg during the corrosion process [13].

Steels that iron (Fe) can become stainless when Fe is alloyed with more than 10 wt.%Cr [14].

Some kinetically passivated metal might also bestow a low corrosion rate by modifying matrix

composition, and changing the amounts and distribution of secondary phases [15]. Hence the

formation of a compact oxide film by alloying with high concentration passivated metals is a

potential strategy to improve corrosion resistance of Mg alloys.

   The main alloying element used in Mg alloys is aluminium (Al). Principally, Al itself is

one of the passivated elements in the atmosphere through the formation of compact Al$_2$O$_3$ film

[16]. The previous results reveal that Al alloying element is of benefit to improve corrosion

resistance of Mg alloys [17, 18]. For the majority of Mg-Al alloys, Al is partly in solid

solution and partly precipitated along dendrite or grain boundaries by forming Mg$_{17}$Al$_{12}$

(β-phase). Therefore, the corrosion performance of Mg-Al alloys is mainly related to Al

distribution and β-phase morphology. Firstly, the corrosion potential of α-matrix is dependent

on the concentration of Al in solid solution [19]. Secondly, β-phase has a more positive

potential than α-phase and this difference may act as a driving force for pitting corrosion [20].

Finally, β-phase may act as a barrier to inhibit corrosion when β-phase forms a fine and

continuous network [12]. Recent results demonstrate that the enrichment of Al-containing

passive film occurs with increasing Al concentration in Mg matrix [19]. Therefore, a high

corrosion resistant Mg-Al alloy would be expected provided that an Al-rich oxide layer can be

attained. However, Al oxides or hydroxides have been not detected in corrosion product layers

in previous works [21]. The preparation of a compact Al-rich oxide layer is still a technical

challenge, partially due to low solubility of Al and low chemical reaction activity of

4

Al-containing compounds.

Herein, a new approach- ultrahigh pressure approach followed by ageing-has been successfully developed to prepare high corrosion resistant Mg alloys. Ultrahigh pressure has firstly been introduced to attain supersaturated solid-solutions. The residual stress is eliminated and fine Al-containing compounds are captured by ageing treatment. Taking Mg-25wt.%Al as a representative system, the ultrahigh solid-solution followed by ageing shows excellent corrosion resistance. This technique has two principal characteristics. i) The concentration of solid-solution Al is very high ($\sim$ 25wt.%) by extending maximum solubility with increasing pressure; both negative difference effect [22] and pitting corrosion can be effectively reduced. ii) Nano-scaled $Mg_{17}Al_{12}$ phases (10-100 nm) with activated high-index planes are captured by ageing treatment, resulting in the formation of Al-rich oxidation film (Al_2O_3: 95 wt.%). We have achieved single-phase Mg-Al binary alloys with outstanding corrosion resistant properties, near to the high purity Mg dependent on three testing methods. These results show a glimmer of light for the development of stainless Mg-based alloys [23].

2. Material and Methods

2.1 Sample preparation

The alloy with a nominal composition of Mg-25Al (wt.%, all following compositions are given in wt.%) was utilized to carry out the experiments. The cast bar with a diameter of 30 mm was prepared by pure raw materials in an electromagnetic induction melting furnace under argon gas atmosphere. The chemical composition of as-cast samples was analyzed by inductively coupled plasma atomic emission spectroscopy (ICP-AES). The main elemental compositions were: Al (25.121%), Si (0.012%), S (0.002%), Fe (0.003%), Cu (0.002%), and

Ni (0.002%), with the balance of Mg.

The cast bar was machined into cylindrical specimens with a diameter of 10 mm and a length of 14 mm for ultrahigh pressure treatment in a modified hexahedral anvil apparatus. The schematic has been shown in our previous work [24]. Firstly, the samples wrapped with tantalum foil were inserted in a BN capsule. The samples were heated in a graphite furnace, and a cubic pyrophyllite was filled as a pressure medium. The samples were treated for 30 min at 800 $^{\circ}$C under ultrahigh pressure of 4 GPa (denoted as USS-Mg-25Al). The loading rate of pressure and the heating rate were 0.2 GPa/min and 10 $^{\circ}$C/s, respectively. The temperature was increased after loading a stable pressure of 4 GPa. After ultrahigh pressure treatment, the samples were quenched to room temperature directly before unloading pressure. Subsequently, an ageing processing was employed to eliminate residual stress. Ageing testing was performed at 150 $^{\circ}$C under atmospheric pressure. The sample after ultrahigh pressure solid-solution and ageing at peak hardness was marked as USSA-Mg-25Al. For comparison, both as-cast (AC-Mg-25Al) and solid-solution treated samples (450 $^{\circ}$C, 12 h) under the protection of Ar gas (SS-Mg-25Al) were involved as references.

2.2 Microstructural observation and produce analysis

The microstructures were performed using a field emission scanning electron microscopy (FESEM). The standard metallographic procedures were applied, including grinding, polishing and etching. The samples were etched in 4% nitric acid alcohol solutions. The elemental concentrations in the matrix and phases were investigated by FESEM equipped with energy dispersive X-ray analysis (EDX) with a system-Oxford INCA device. A loading voltage of 8 keV with a spot of ~1 μm in diameter was used to study the phase composition. The average

values were obtained based on at least five random spots.

The phase composition was studied by X-ray diffraction (XRD). XRD was achieved with a CuK_α radiation at a scan scope from 20° to 80° with a step size of 0.02°. The filament current and acceleration voltage were 100 mA and 40 kV, respectively. In addition, the $\sin^2\psi$ method of XRD technique was performed for residual stress evaluation [25], where ψ were 0°, 10°, 20°, 30° and 40°. The samples were electro-polished before testing, and the (102) peak rang of 36.5~38.9° was selected for stress calculation.

The samples were immersed in 3.5 wt.%NaCl for 5, 60 and 360 min, and then dried in a vacuum for testing. The intersection microstructure was investigated by optical microscopy (OM) and FESEM. The phase composition of the samples immersed for 360 min were confirmed by X-ray photoelectron spectroscopy (XPS), which was performed with a spectrometer equipped with an MgK_α ray source (1253.6 eV protons).

2.3 Electrochemical testing

Corrosion performance was evaluated using a potentiostat/frequency response analysis system (Bio-logic, VSP). Experiments were performed in a three-electrode electrochemical cell in 3.5 wt.% NaCl solutions at room temperature, with a saturated calomel electrode (SCE) as the reference electrode, a platinum mesh as the counter electrode and the specimen under investigation as the working electrode. The working electrodes were ground with silicon carbide paper to 3000 grit and then rinsed with distilled water and degreased with ethanol and acetone. The distance between the three electrodes is about 1.5 cm, and the ratio of solution to surface is 600 mL to 0.5 cm^2. The reaction was stirred at a speed of 150 rpm.

Open circuit potential (OCP) measurements were carried out between the working

electrode and the reference electrode without current. The OCP were tested immediately after

the specimens were immersed in the solutions, and were measured for 4 h duration. The

polarization curves were performed from -1.7 V (*vs.* SCE) to -0.4 V (*vs.* SCE) on the samples

after immersing them for 4 h. The scan rate was 0.166 mV/s and the step height was 1 mV.

These experiments were continuously scanned five times to investigate average corrosion

resistance and film recovery ability when it was destroyed. After scanning, an interval of 2 h

was performed to form a new oxidation layer and also to reduce the effect of previous

scanning. The electrochemical impedance spectroscopy (EIS) was carried out at open circuit

potential with an applied signal of 10 mV/rms. The scanning frequency ranged from 100 kHz

to 0.1 Hz. The fitting circuits were achieved by EC-Lab software. The EIS testing was

performed on the different samples after immersing them for 2, 4 and 6 h, respectively.

2.4. Corrosion evaluation

The corrosion properties of cylinder samples with a diameter of 8 mm and a height of 3 mm

were evaluated by Tafel extrapolation (P_i), weight loss (P_w) and hydrogen evolved during

corrosion (P_h). The polarization curve was used to estimate corrosion potential (E_{corr}), and

corrosion current density (i_{corr}) at corrosion potential (E_{corr}) by the Levenburg-Marquardt (LEV)

method [26] as follows:

$$i = i_{corr}(10^{\frac{E-E_{corr}}{\beta_a}} - 10^{\frac{E-E_{corr}}{\beta_c}})\tag{1}$$

β_a and β_c are the anodic and cathodic Tafel slopes. LEV fitting is able to provide a value

of the anodic Tafel slope. Therefore, the corrosion current density was derived from the

polarization resistance [26] (R_p):

$$i_{corr} = \frac{\beta_c\beta_a}{2.3R_p(\beta_a - \beta_c)}\tag{2}$$

The instantaneous corrosion rate from polarization curves, P_i (mm/y), is determined from the i_{corr} (A/cm^2) using [5]:

$$P_i = 22.85 i_{corr} \qquad (3)$$

Curves were performed five times to calculate the average P_i values.

In the case of weight loss testing, the corrosion products were removed through immersion in chromic acid (20wt.% CrO_3 + 2wt.% $AgNO_3$) until there was no visible reaction. Each specimen was washed with water, ethanol and dried with hot air. The corrosion rates from weight loss, P_w (mm/y), were evaluated using [5]:

$$P_w = 2.1 \, \Delta w / At \qquad (4)$$

where Δw is the decrease in weight (mg), A is the average exposed surface area (cm^2), and t is the immersion time (y). Three different samples were carried out for calculating average P_w.

The corrosion rates from the evolved hydrogen, P_H (mm/y), were evaluated using [5]:

$$P_H = 2.088 \, V_H / At \qquad (5)$$

where V_H is the volume of hydrogen evolved (mL), A is the exposed surface area (cm^2), and t is the immersion time (y). Each sample condition was tested in triplicate to reduce experimental error.

3. Results

3.1 Microstructural characterization

Fig. 1a shows a typical microstructure of AC-Mg-25Al alloy, in which a wide band of secondary phase is distributed in dendrite boundaries. The Al concentrations in the pots A and B are 9.1 wt.% and 31.3 wt.%, respectively. According to the Mg-Al binary phase diagram, it can be confirmed that the pots A and B correspond to Mg matrix and $Mg_{17}Al_{12}$ eutectic phase

under equilibrium solidification [27], which is consistent with conventional as-cast

Mg-Al-based alloys [21]. In contrast, a similar morphology is detected after atmospheric

solid-solution treatment (**Fig. 1b,** SS-Mg-25Al), wherein the pots C and D change to 13.5

wt.% and 30.4 wt.%, respectively. It agrees well with the rapid solidification in terms of phase

diagram [27]. However, a simple phase of equiaxial structure has been detected after ultrahigh

pressure solid-solution (4 GPa, 800 $^{\circ}$C) (**Fig. 1c,** USS-Mg-25Al). The secondary phase is

eliminated and the Al concentration in Mg matrix is 24.9 wt.%, which is far higher than that of

the solid-solution treated sample (~13.5 wt.%). Although the macro-structure of the

USSA-Mg-25Al (**Fig. 1d**) remains similar to that of the USSed sample, an obvious ageing

hardening response occurs at 150 $^{\circ}$C (**Fig. 1e**), in which the average microhardness increases

from 106 HV to 186 HV. The concentration of Al in Mg matrix reduces to ~ 20.1 wt.%, which

is far higher than that of the as-cast sample (~9.1 wt.%) . Compared with other traditional

ageing hardening Mg alloys (20-150 h [1]), the ageing time for reaching to the peak hardness

(~3 h) sharply shortens owing to the existence of a large stress field. This trend of phase

transformation is further confirmed by the XRD patterns (**Fig. 1f**). It demonstrates that the

reason for ageing hardening is associated with the reappearance of β-$Mg_{17}Al_{12}$ phase, wherein

the particle dimension is ~40 nm calculated by the Scherrer formula [28].

To further probe the reason of ageing hardening, TEM and HRTEM observations were

performed on the USSA-Mg-25Al sample. Specifically, two different precipitates (trip-like

particle A and dot-like particle B**, Fig. 2a**) are observed. The local high magnification image

(**Fig. 2b**) reveals that the trip-like particle A is composed of several fine plate-shaped

precipitates. The precipitate has been confirmed to be $Mg_{17}Al_{12}$ in terms of the SEAD pattern,

and an orientation relationship of $(0002)_m//(01\text{-}1)_\beta$, $[2\text{-}1\text{-}10]_m//[\text{-}111]_\beta$, is identified. The

HRTEM image (**Fig. 2c-d**) shows that a large number of fine precipitates (particle B) are

homogeneously distributed in the matrix. The lattice spaces are consistent with the standard

values of $Mg_{17}Al_{12}$ (PDF#01-1128), in which some high-index planes of {422}, {721} and

{510} are captured. In addition, the average sizes of coarse particle A and fine particle B are ~

100 nm and ~ 10 nm, respectively (**Fig. 2e**). The particle size calculated by the Scherrer

formula is different from that measured by TEM observation. The reason is that the XRD

patterns reflect an average bulk value, whilst TEM result generally represents a local area.

The Mg-Al phase diagram reveals the difficulty in achieving supersaturated

solid-solution alloys using the common heat-treatment method owing to a high solubility of Al

in Mg matrix. Specifically, when the Al concentration is higher than the equilibrium value,

large-scale $Mg_{17}Al_{12}$ compounds occurs, decreasing ductility and corrosion resistant properties.

As a result, the ageing hardening response is hardly reported in Mg-Al binary alloys. Herein

we have reported superfine $Mg_{17}Al_{12}$ particles (10-100 nm) by ultrahigh pressure

solid-solution followed by ageing. Three advantages can be identified when compared with

conventional Mg-Al based alloys. On one hand, differing from previous coarse $Mg_{17}Al_{12}$

eutectic phase (ten micrometers [29]) or deformed alloys (several micrometers [30]), the

nano-scaled $Mg_{17}Al_{12}$ particles can act as strengthening cores for prohibiting dislocation

motion [31] and improving microhardness. On the other hand, with increasing Al

concentration in Mg matrix, the potential gap between Mg matrix and β phase becomes narrow,

weakening localized corrosion. Thus, the interface stress shield between the secondary phase

and matrix will be reduced substantially, increasing the stability of the oxide film. Finally, a

large number of high-index planes are achieved instead of low-index planes (closed planes).

These high-index planes bestow higher chemical activity in contrast to low-index planes

during corrosion process [32], offering a prerequisite to form a uniform Al-rich oxide film.

3.2 Electrochemical corrosion properties

Fig. 3a shows open circuit potential (OCP) as a function of immersion time (4 h) in 3.5

wt.% NaCl aqueous solution at room temperature. In principal, the potentials continuously

increase by increasing immersion time. In the cases of the AC-Mg-25Al and SS-Mg-25Al

alloys, apparent fluctuating potentials are detected during the whole testing range. A sharp

drop illustrates that the preliminary passive film on these samples broke down suddenly. By

comparison, relatively smooth curves are confirmed in the USS-Mg-25Al and

USSA-Mg-25Al alloys. Note that the USSA-Mg-25Al alloy merely took about 3 min to reach

an equilibrium potential of -1.29 V, indicating the formation of stable passive films.

Five potentiodynamic polarization tests of different state Mg-25Al alloys have been

performed continuously (**Fig 3b-e**). The corresponding average parameters are listed in Table

2. The other three alloys except for the USSA-Mg-25Al alloy show a similar electro-chemical

process. An apparent passivation platform is detected in the initial anode branch at the Tafel

curves. However, the passivation platform is weak or eliminated with increased scanning

numbers, suggesting the formation of an oxide film during corrosion process which cannot

prohibit the medium penetration. In contrast, the similar Tafel curves are observed in the

USSA-Mg-25Al alloy, in which the repeated vertical anode branches are attained. Not only

does it imply that the formation of the oxide layer is closed, but also the oxide film can be

rapidly regenerated after it is broken by a large polarization current during the polarization

12

cycle testing.

The corrosion process has been investigated by EIS tests. The Nyquist spots and Bode spectra have been carried out on the different samples immersed in 3.5 wt.% NaCl aqueous solutions for different times. The AC-Mg-25Al, SS-Mg-25Al and USS-Mg-25Al samples (**Fig. 4a-d and Fig. 5**) present a high frequency (100-10 kHz) resistive behaviour followed by a high capacitive response, and a distorted inductance loop at medium/low frequencies (1-0.1 Hz). However, only a capacitive semi-circle is observed in the USSA-Mg-25Al alloy. The EIS spectra have been analyzed with respect to equivalent circuits (**Fig. 4i-j**), where R_s represents the solution resistance; R_{ct} and R_L represent the charge transfer resistance and the inductance resistance, respectively. Two *CPE*s are constant phase elements for compensating the non-homogeneity in the system. CPE_{dl} is related to the electric double layer at the interface of the electrolyte solution and the alloy substrate. CPE_l (inductive behaviour) is generally attributed to high concentration of Mg ions on relatively film-free areas or an intermediate step in the corrosion process involving the presence of adsorbed surface species. In addition, the existence of an inductive loop commonly implies the occurrence of pitting corrosion [33].

Differing from the other three samples, the fitting results (**Table 3**) display the value of R_{ct} of the USSA-Mg-25Al alloy increases with increasing immersion time, implying a decreased dissolution rate. In particular, the high value of R_{ct} after immersion for 6 h is $\sim 6 \times 10^4$ ohm cm^2, which is near to the value of Al_2O_3 ($\sim 10^3$ ohm cm^{-2} [34]), revealing the formation of the closed oxide layer. The absence of the inductive loop indicates that the oxide layer effectively hinders the solution penetration.

3.3 Corrosion rate

Based on Tafel polarization curves, the average corrosion rate (P_i) of the testing samples is calculated (**Table 2**). The average value of the USSA-Mg-25Al alloy is ~ 0.14 mm/y, which is 2.5% of the AC-Mg-25Al alloy. To the best our knowledge, the corrosion current density outperform the majority of commercial Mg-based alloys reported so far [35-42] (**Fig. 6**). However, as confirmed by Shi and Atrens [43], Tafel extrapolation has typically been used to measure initial corrosion behaviour, and this initial corrosion behaviour may not be associated with steady-state corrosion behaviour. Therefore, weight loss and hydrogen evolution have been further performed to investigate their corrosion properties. All specimens/treatments studied herein were immersed in quiescent 3.5wt.% NaCl for 6 days in order to determine the long-term corrosion properties. The results from weight loss testing are shown in **Fig. 7**. A lowest corrosion rate of ~0.44 mm/y is achieved for the USSA-Mg-25Al alloy, which is approximate a tenfold improvement in contrast to the AC-Mg-25Al and SS-Mg-25Al alloys. Attractively, the value is slightly larger than those of superhigh purity Mg of ~0.25 mm/y [26] and high purity Mg of ~0.38 mm/y [5].

The evolved hydrogen over the duration is shown in **Fig. 8a**, and the average corrosion rate is presented in **Fig. 8b.** Differing from continuously increased hydrogen volume for the other three samples, a stable platform is observed in the USSA-Mg-25Al alloy during the immersion testing, resulting in the lowest corrosion rate (~2.21 mm/y). Note that this corrosion rate is larger than that of superhigh purity Mg of ~0.53 mm/y [26], but near to that of high purity Mg of ~2.10 mm/y [5, 44]. According to the aforementioned three methods, we can confirm that the ultrahigh pressure following by ageing is one of the most effective approaches for improving the corrosion properties of Mg-Al alloys. The corrosion properties

of the USSA-Mg-25Al alloy are better than the majority of Mg alloys, and near to that of high purity Mg.

4. Discussion

To understand corrosion process, *ex-situ* SEM observations after immersion for different intervals were performed. For the AC-Mg-25Al alloy, the corrosion phenomenon occurs immediately. Some filamentous oxides are detected on the surface of the sample after being immersed for 5 min (**Fig. 9a**). As the immersion time increases (60 min, **Fig. 9b**), some severe pitting corrosion dots, cracks, holes and petals-shaped oxides are observed on the surface. A high-magnification image shows that when the matrix is removed to a significant extent, a wide gap is formed owing to different stress conditions between the coarse secondary phase and the matrix, resulting in a cracked oxide film. Additionally, a fresh surface is detected under the cracks (**Fig. 9b-3**), suggesting a weak regeneration ability. By comparison, the surface of the USSA-Mg-25Al alloy is maintained smooth even after immersing for 360 min apart from a few scattered etched spots (**Fig. 9c-d**). A compact oxide film is also observed even in the core of small gap owing to the high chemical reaction activity of nano-scaled $Mg_{17}Al_{12}$ and supersaturated Al in the Mg. This similar phenomenon is reported in nano-sized Mg-Zn based alloys, in which fine particles containing Zn result in the rapid formation of oxide layer [45].

In addition, after being immersed for 360 min, the irregular inter-cross structure of the SS-Mg-25Al alloy (**Fig. 10a**) shows that the block secondary phase is stripped away as the supporting matrix disappears during the corrosion process, resulting in the increment of corrosion rate (negative different effect: NDE [22]). In turn, the NDE is restrained for the

simple-phase sample, and the uniformed surfaces are attained due to the unanimous corrosion rate. Notably, differing from the USSA-Mg-25Al sample, a twin band with a width of 150-200 nm is observed near to the surface of the USS-Mg-25Al sample (**Fig. 10b**). The wide twins are mainly related to the highest residual stress based on XRD testing (**Fig. 10c-d**) [46]. By increasing the concentration of solid solution atom, the stress is enhanced greatly. When the oxide film on the surface is formed, the residual stress is released. Thus the neighbour grains are compressed, leading to the occurrence of twins. The twin deformation during the corrosion process readily breaks the surface oxide layer, varying the OCP and accelerating corrosion.

Finally, the film structure plays a critical role in enhancing corrosion resistance except for the aforementioned two reasons. The chemical composition of oxide layer is investigated by XPS tests (**Fig. 11**). The fitting results of O_{1s} peak show that the oxide layer of the USSA-Mg-25Al sample is mainly composed of a Al-rich layer (Al_2O_3: ~95 wt.%). However, the other samples chiefly consist of a common Mg-rich layer (MgO: ~52 wt.%). The aggregation reason of Al instead of Mg is another interesting issue, and will be further discussed elsewhere in the future. Compared with Mg-rich oxidation film, the Al-rich layer is more compact, remarkably improving corrosion resistant properties. It is believed that the excellent corrosion resistant performance is mainly related to the presence of the compact Al-rich oxide film.

5. Conclusions

The microstructure and corrosion properties of different state Mg-25Al binary alloys have been investigated. The following conclusions have been drawn:

(1) Ultrahigh pressure is an effective approach to obtain supersaturated solid-solution Mg-Al

16

alloys, which might achieve high mechanical properties by ageing hardening response.

(2) A large residual stress remains after ultrahigh pressure. It accelerates ageing precipitate

kinetics, but deteriorates corrosion resistance by breaking the oxide layer due to the

formation of twin bands.

(3) Mg-25Al alloy after ultrahigh pressure and ageing shows unique corrosion resistance.

The corrosion properties of the USSA-Mg-25Al alloy were better than the majority of

bare Mg-based alloys, and near to that of high purity Mg.

(4) The reasons for high corrosion resistant properties are mainly related to the presence of

Al-rich oxide film, wherein pitting corrosion, negative difference effect and residual

stress are significantly reduced.

Acknowledgment

References

[1] K.U. Kainer, Magnesium alloys and their applications, Wiley-VCH, 1999.

[2] X. Liu, T. Zhang, Y. Shao, G. Meng, F. Wang, Effect of alternating voltage treatment on the corrosion resistance of pure magnesium, Corr. Sci. 51 (2009) 1772-1779.

[3] S. Johnston, Z. Shi, M.S. Dargusch, A. Atrens, Influence of surface condition on the corrosion of ultra-high-purity Mg alloy wire, Corr. Sci. 108 (2016) 66-75.

[4] S. Thomas, N.V. Medhekar, G.S. Frankel, N. Birbilis, Corrosion mechanism and hydrogen evolution on Mg, Curr.Opin. Solid State Mater. Sci. 19 (2015) 85-94.

[5] F. Cao, G.L. Song, A. Atrens, Corrosion and passivation of magnesium alloys, Corr. Sci. 111 (2016) 835-845.

[6] K. Schlüter, Z. Shi, C. Zamponi, F. Cao, E. Quandt, A. Atrens, Corrosion performance and mechanical properties of sputter-deposited Mg-Y and Mg-Gd alloys, Corr. Sci. 78 (2014) 43-54.

[7] Atrens A., Song G.L., Liu M., Shi Z. , Cao F., Dargusch M.S., Review of recent developments in the field of magnesium corrosion, Adv. Eng. Mater. 17 (2015) 400-453.

[8] S.V. Lamaka, M.F. Montemor, A.F. Galio, M.L. Zheludkevich, C. Trindade, L.F. Dick, M.G.S. Ferreira, Novel hybrid sol–gel coatings for corrosion protection of AZ31B magnesium alloy, Electrochem. Acta 53 (2008) 4773-4783.

[9] Y. Tamar, D. Mandler, Corrosion inhibition of magnesium by combined zirconia silica sol–gel films, Electrochem. Acta 53 (2008) 5118-5127.

[10] Y.W. Song, D.Y. Shan, E.H. Han, Corrosion behaviors of electroless plating Ni–P coatings deposited on magnesium alloys in artificial sweat solution, Electrochem. Acta 53 (2007) 2009-2015.

[11] C.E. Barchiche, E. Rocca, C. Juers, J. Hazan, J. Steinmetz, Corrosion resistance of plasma-anodized AZ91D magnesium alloy by electrochemical methods, Electrochem. Acta 53 (2007) 417-425.

[12] A.Atrens. G. Song, Corrosion mechanisms of magnesium alloys, Adv. Eng. Mater., (1999) 11-33.

[13] M. Esmaily, J.E. Svensson, S. Fajardo, N. Birbilis, G.S. Frankel, S. Virtanen, R. Arrabal, S. Thomas, L.G. Johansson, Fundamentals and advances in magnesium alloy corrosion, Prog. Mater. Sci. 89 (2017) 92-193.

[14] S. Jiang, F. Chai, H. Su, C. Yang, Influence of chromium on the flow-accelerated corrosion behavior of low alloy steels in 3.5% NaCl solution, Corr. Sci. 123 (2017) 217-227.

[15] X. Qi, H. Mao, Y. Yang, Corrosion behavior of nitrogen alloyed martensitic stainless steel in chloride containing solutions, Corr. Sci. 120 (2017) 90-98.

[16] R.M. Bandeira, J. van Drunen, A.C. Garcia, G. Tremiliosi-Filho, Influence of the thickness and roughness of polyaniline coatings on corrosion protection of AA7075 aluminum alloy, Electrochem. Acta, 240 (2017) 215-224.

19

[17] R. Xu, X. Yang, K.W. Suen, G. Wu, P. Li, P.K. Chu, Improved corrosion resistance on

biodegradable magnesium by zinc and aluminum ion implantation, Appl. Surf. Sci. 263 (2012)

608-612.

[18] P. Casajús, N. Winzer, Electrochemical noise analysis of the corrosion of high-purity Mg–Al

alloys, Corr. Sci. 94 (2015) 316-326.

[19] M. Danaie, R.M. Asmussen, P. Jakupi, D.W. Shoesmith, G.A. Botton, The role of aluminum

distribution on the local corrosion resistance of the microstructure in a sand-cast AM50 alloy,

Corr. Sci. 77 (2013) 151-163.

[20] S. Mathieu, C. Rapin, J. Steinmetz, P. Steinmetz, A corrosion study of the main constituent

phases of AZ91 magnesium alloys, Corr. Sci. 45 (2003) 2741-2755.

[21] M. Jönsson, D. Persson, C. Leygraf, Atmospheric corrosion of field-exposed magnesium alloy

AZ91D, Corr. Sci. 50 (2008) 1406-1413.

[22] S. Lebouil, A. Duboin, F. Monti, P. Tabeling, P. Volovitch, K. Ogle, A novel approach to on-line

measurement of gas evolution kinetics: application to the negative difference effect of Mg in

chloride solution, Electrochem. Acta, 124 (2014) 176-182.

[23] G.L. Song, A. Atrens, Understanding magnesium corrosion mechanism: a framework for

improved alloy performance, Adv. Eng. Mater. 5(2003) 837-858.

[24] H. Fu, B. Ge, Y. Xin, R. Wu, C. Fernandez, J. Huang, Q. Peng, Achieving high strength and

ductility in magnesium alloys via densely hierarchical double contraction nanotwins, Nano Lett.

17 (2017) 6117-6124.

[25] Y.F. Li, B. Yao, Y.M. Lu, Y.Q. Gai, C.X. Cong, Z.Z. Zhang, D.X. Zhao, J.Y. Zhang, B.H. Li,

D.Z. Shen, X.W. Fan, Z.K. Tang, Biaxial stress-dependent optical band gap, crystalline, and

electronic structure in wurtzite ZnO: experimental and ab initio study, J. Appl. Phys. 104 (2008) 083516.

[26] F. Cao, Z. Shi, J. Hofstetter, P.J. Uggowitzer, G. Song, M. Liu, A. Atrens, Corrosion of ultra-high-purity Mg in 3.5% NaCl solution saturated with $Mg(OH)_2$, Corr. Sci. 75 (2013) 78-99.

[27] M. Liu, P.J. Uggowitzer, A.V. Nagasekhar, P. Schmutz, M. Easton, G.-L. Song, A. Atrens, Calculated phase diagrams and the corrosion of die-cast Mg–Al alloys, Corr. Sci. 51 (2009) 602-619.

[28] A.L. Patterson, The Scherrer formula for X-ray particle size determination, Phys. Rev. 56 (1939) 978-982.

[29] S. Seetharaman, C. Blawert, B.M. Ng, W.L.E. Wong, C.S. Goh, N. Hort, M. Gupta, Effect of erbium modification on the microstructure, mechanical and corrosion characteristics of binary Mg–Al alloys, J. Alloys Compd. 648 (2015) 759-770.

[30] H. Wang, K. Zhou, G. Xie, X. Liang, W. Liang, Y. Zhao, Microstructure and mechanical properties of an Mg-10Al alloy fabricated by Sb-alloying and ECAP processing, Mater. Sci. Eng. A, 560 (2013) 787-791.

[31] J.F. Nie, Effects of precipitate shape and orientation on dispersion strengthening in magnesium alloys, Scr. Mater. 48 (2003) 1009-1015.

[32] N. Tian, Z.Y. Zhou, S.-G. Sun, Y. Ding, Z.L. Wang, Synthesis of tetrahexahedral platinum nanocrystals with high-index facets and high electro-oxidation activity, Science, 316 (2007) 732-735.

[33] O.P. Watts, The electrochemical theory of corrosion, transactions of the electrochemical society, 64 (1933) 125-153.

[34] A.A. Minea, R.S. Luciu, Investigations on electrical conductivity of stabilized water based Al$_2$O$_3$ nanofluids, Microfluid. Nanofluid. 13 (2012) 977-985.

[35] L. Wang, K. Zhang, W. Sun, T. Wu, H. He, G. Liu, Hydrothermal synthesis of corrosion resistant hydrotalcite conversion coating on AZ91D alloy, Mater. Lett. 106 (2013) 111-114.

[36] A.D. Südholz, N. Birbilis, C.J. Bettles, M.A. Gibson, Corrosion behaviour of Mg-alloy AZ91E with atypical alloying additions, J. Alloys Compd. 471 (2009) 109-115.

[37] K. Gusieva, C.H.J. Davies, J.R. Scully, N. Birbilis, Corrosion of magnesium alloys: the role of alloying, Int. Mater. Rev. 60 (2015) 169-194.

[38] Y. Cheng, T. Qin, H. Wang, Z. Zhang, Comparison of corrosion behaviors of AZ31, AZ91, AM60 and ZK60 magnesium alloys, Trans. Nonferrous Met. Soc. China, 19 (2009) 517-524.

[39] W.C. Say, C.C. Chen, S.J. Hsieh, Electrochemical characterization of non-chromate surface treatments on AZ80 magnesium, Mater. Character. 59 (2008) 1400-1406.

[40] D. Cao, L. Wu, Y. Sun, G. Wang, Y. Lv, Electrochemical behavior of Mg–Li, Mg–Li–Al and Mg–Li–Al–Ce in sodium chloride solution, J. Power Sources, 177 (2008) 624-630.

[41] Y.K. Wei, Y.J. Li, Y. Zhang, X.T. Luo, C.J. Li, Corrosion resistant nickel coating with strong adhesion on AZ31B magnesium alloy prepared by an in-situ shot-peening-assisted cold spray, Corr. Sci. 138 (2018) 105-115.

[42] G.-L. Song, R. Mishra, Z. Xu, Crystallographic orientation and electrochemical activity of AZ31 Mg alloy, Electrochem. Commun. 12 (2010) 1009-1012.

[43] Z. Shi, A. Atrens, An innovative specimen configuration for the study of Mg corrosion, Corr. Sci. 53 (2011) 226-246.

[44] Z. Shi, J.X. Jia, A. Atrens, Galvanostatic anodic polarisation curves and galvanic corrosion of high purity Mg in 3.5% NaCl saturated with Mg(OH)$_2$, Corr. Sci. 60 (2012) 296-308.

[45] Y. Lu, A.R. Bradshaw, Y.L. Chiu, I.P. Jones, Effects of secondary phase and grain size on the corrosion of biodegradable Mg–Zn–Ca alloys, Mater. Sci. Eng. C, 48 (2015) 480-486.

[46] T. Hosaka, S. Yoshihara, I. Amanina, B.J. MacDonald, Influence of grain refinement and residual stress on corrosion behavior of AZ31 magnesium alloy processed by ECAP in RPMI-1640 medium, Procedia Eng. 184 (2017) 432-441.

Table 1. Elemental compositions of different positions in Fig. 1.

wt.%	Positions					
	A	B	C	D	E	F
Al	9.1±0.12	31.3±0.21	13.5±0.14	30.4±0.31	24.9±0.11	20.1±0.21

Table 2. The parameters calculated on Tafel curves in terms of five results.

Samples	E_{corr} (V/SCE)	i_{corr} (A/cm^2)	β_a (V/dec)	β_c (V/dec)	P_i (mm/y)
AC-Mg-25Al	-1.33 ± 0.06	$2.4\pm0.2\times10^{-4}$	0.56 ± 0.15	-0.17 ± 0.02	5.48 ± 0.15
SS-Mg-25Al	-1.24 ± 0.05	$3.4\pm0.4\times10^{-4}$	0.25 ± 0.08	-0.23 ± 0.03	7.56 ± 0.22
USS-Mg-25Al	-1.19 ± 0.04	$5.2\pm0.4\times10^{-5}$	0.24 ± 0.04	-0.18 ± 0.01	1.19 ± 0.28
USSA-Mg-25Al	-1.23 ± 0.03	$6.2\pm0.3\times10^{-6}$	2.81 ± 0.06	-0.16 ± 0.02	0.14 ± 0.11

ACCEPTED MANUSCRIPT

Table 3. The fitting results of the EIS curves.

Samples	Time h	R_s ohm cm^2	CPE_l μF cm^{-2}	R_L ohm cm^2	L μH cm^{-2}	R_t ohm cm^2
AC-Mg-25Al	2	22.1	18.0	34.1	1.3×10^9	90.6
	4	25.1	51.4	9.8	2.3×10^8	18.3
	6	24.6	103.4	7.8	5.2×10^8	18.2
SS-Mg-25Al	2	14.1	11.6	41.6	4.2×10^8	63.1
	4	11.6	38.3	6.6	1.8×10^8	11.7
	6	12.3	54.2	22.0	5.8×10^7	10.3
USS-Mg-25Al	2	24.2	11.1	127.3	1.2×10^9	113.4
	4	25.7	34.5	17.9	2.2×10^8	18.9
	6	27.0	42.1	19.4	2.3×10^8	21.4
USSA-Mg-25Al	2	31.0	9.1	-	-	681.6
	4	32.3	17.2	-	-	33691.9
	6	48.3	16.6	-	-	59549.2

26
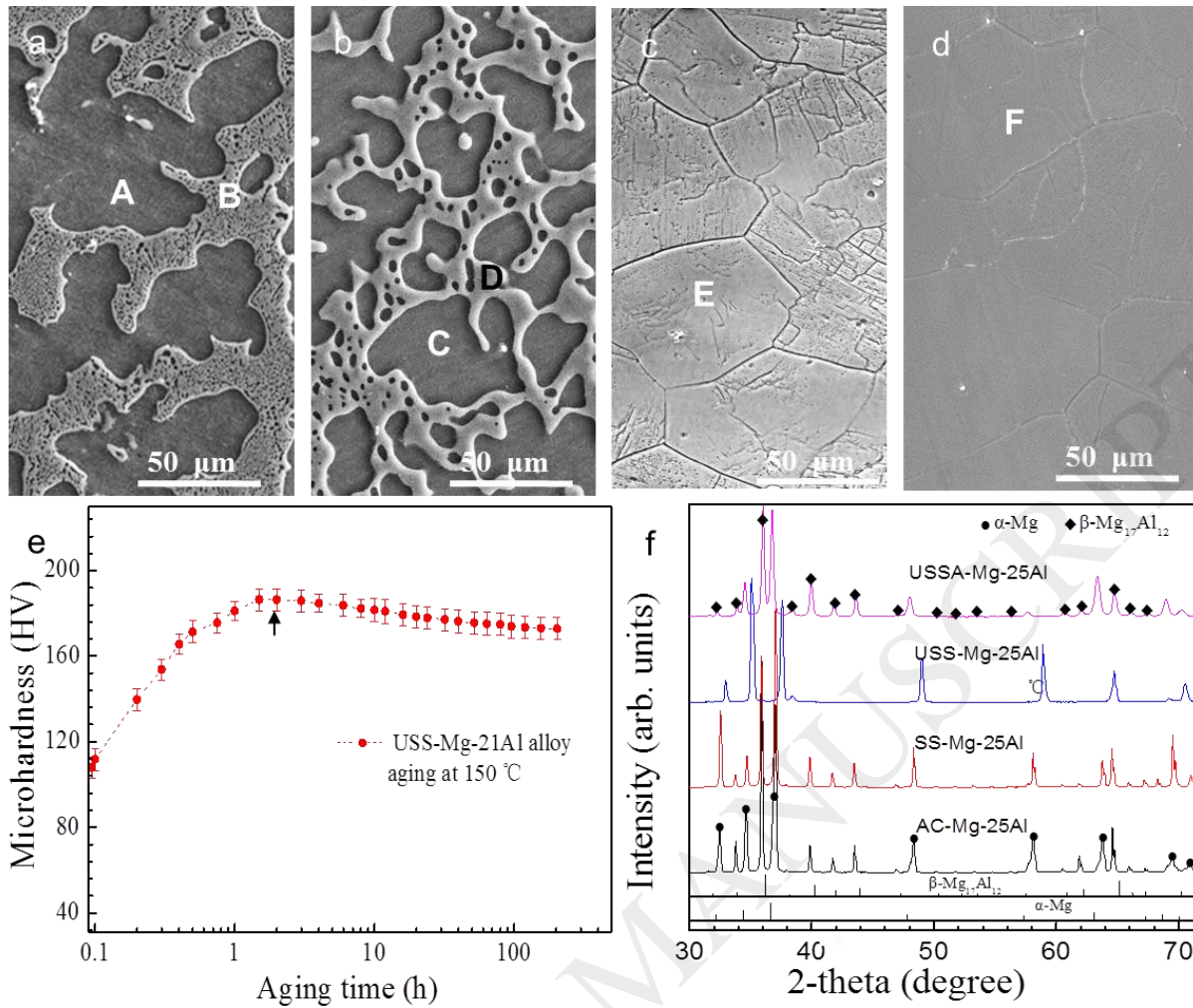
Figure 1. Microstructure and phase composition. SEM images of the samples under different

states, (a) pristine AC-Mg-25Al; (b) SS-Mg-25Al; (c) USS-Mg-25Al; (d) USSA-Mg-25Al. (e)

Ageing curve of the USS-Mg-25Al at 150 ^{o}C. A typical age-hardening response is confirmed

for ~3 h. (f) XRD patterns of different state Mg-25Al samples. The peaks of eutectic β phase

are fully eliminated after ultrahigh pressure treatment (4 GPa, 800 ^{o}C).
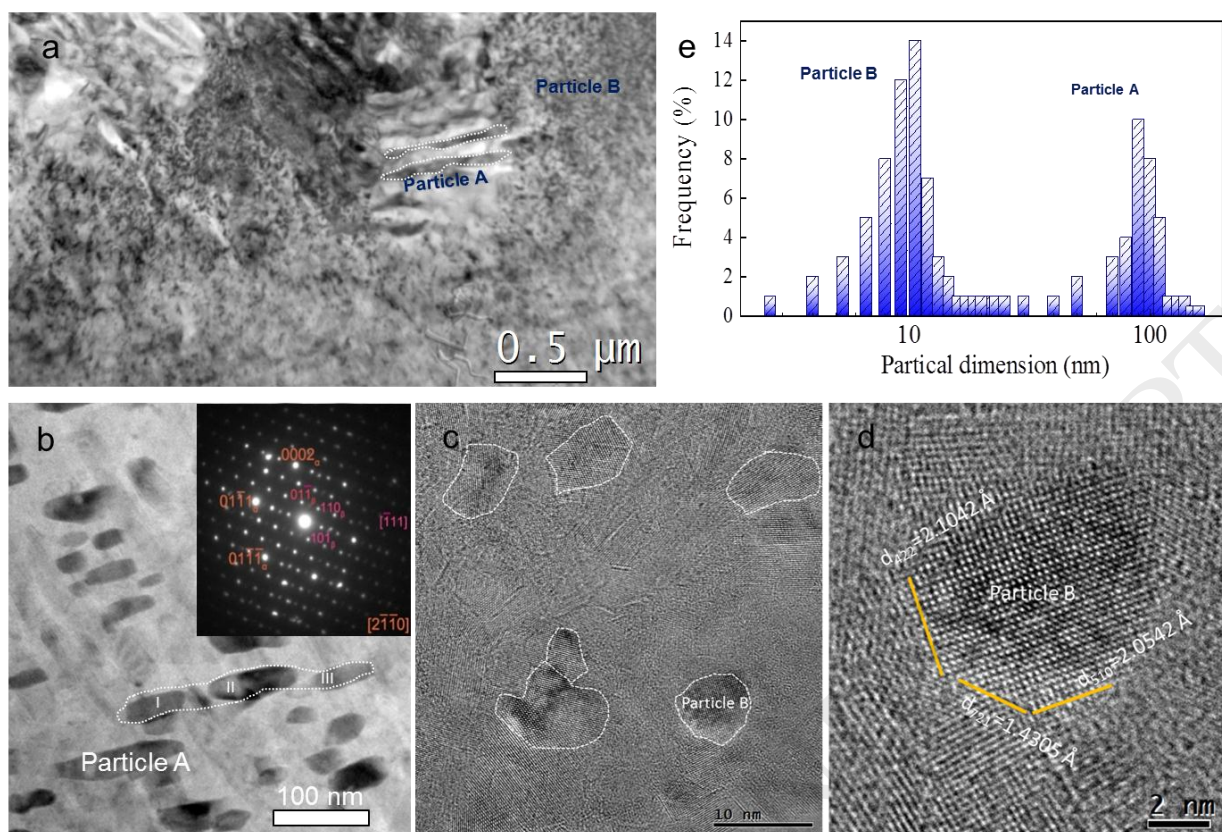
Figure 2. Microstructural characterization of the USSA-Mg-25Al sample. (a) TEM image of the USSA-Mg-25Al sample. Two different structures (particles A and B) are observed. (b) Typical high magnification TEM image of particle A, the inset corresponds to its SEAD pattern along $[2\bar{1}\bar{1}0]$ and typical low-index planes of {110} are observed. (c) Typical high magnification TEM image of particle B with the dimension of ~10 nm. (d) HRTEM image of particle B. Some high-index planes of {422}, {721} and {510} are captured. (e) Dimension distribution of particles A and B.
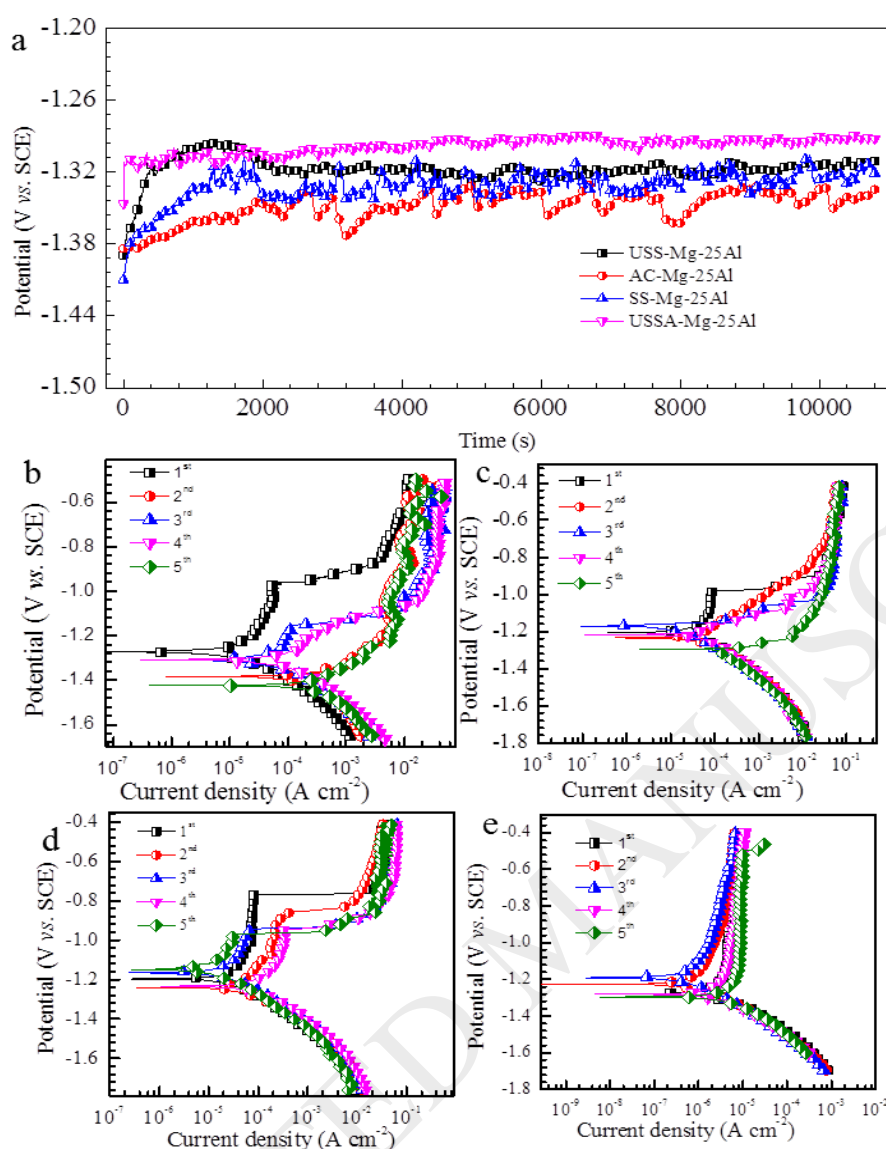
Figure 3. OCP and Tafel curves. (a) Open circuit potential curves of the Mg-25Al alloys under different states for 4 h, 10 spots skipped. Five continuous Tafel curves of the Mg-25Al alloys under different states at a scan rate of 0.166 mV/s in 3.5 wt.% NaCl solution . (b) AC-Mg-25Al; (c) SS-Mg-25Al; (d) USS-Mg-25Al; (e) USSA-Mg-25Al. An interval of 2 h between two tests was performed to form a new oxidation layer and to reduce the effect of previous scanning.

29
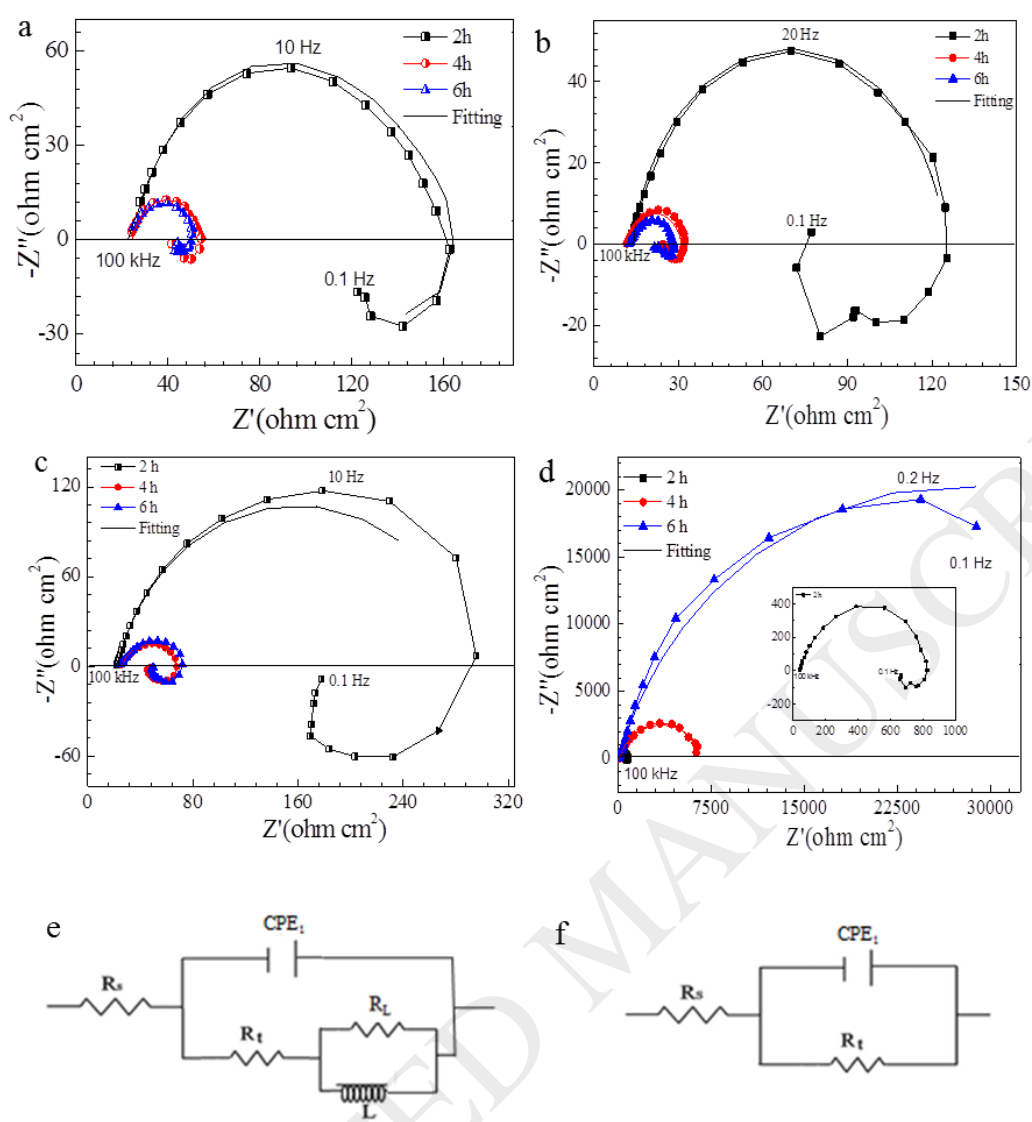
Figure 4. Nyquist curves of the Mg-25Al alloys in different states immersed in 3.5 wt.% NaCl

solution for different immersion times, (a) AC-Mg-25Al; (b) SS-Mg-25Al; (c) USS-Mg-25Al;

(d) USSA-Mg-25Al. The smooth lines are the fitted ones according to the equivalent circuit. (e)

The fitting circuit for (a), (b) and (c). (f) The fitting circuit for (d).
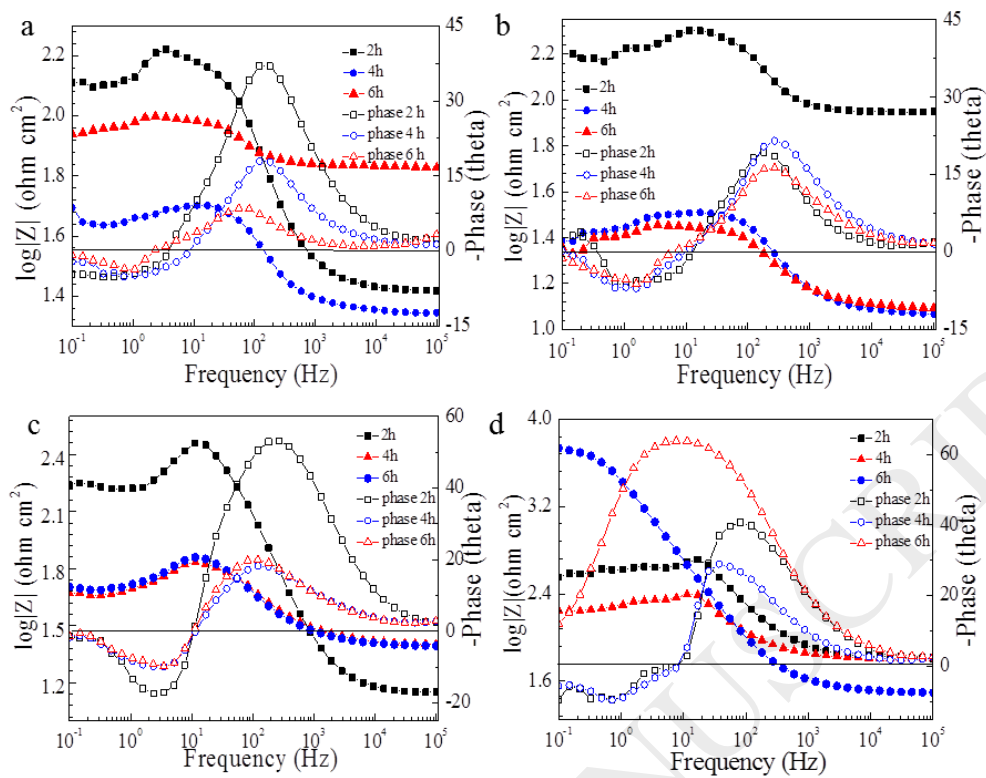
Figure 5. Bode spectra of the different state Mg-25Al alloys immersed in 3.5 wt.% NaCl

solution for different immersion times.

31
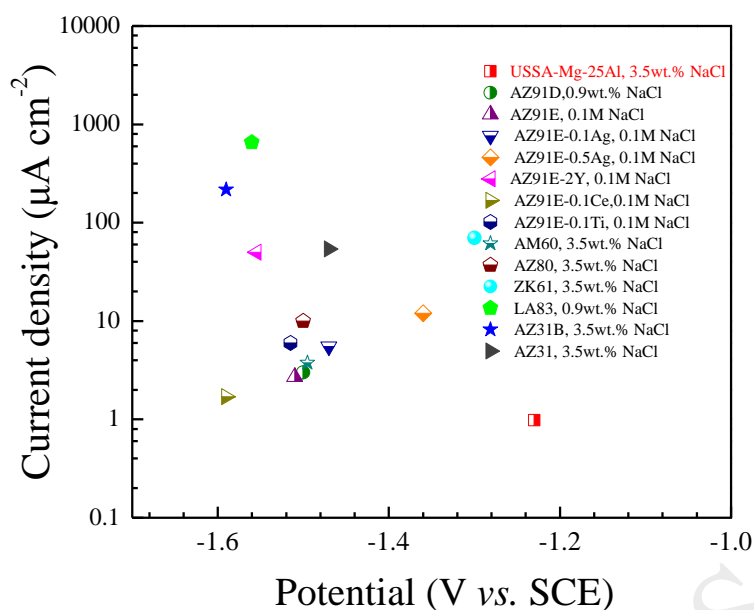
Figure 6. Comparative current density-potential data of the main Mg-based alloys reported so

far. The corrosion current densities of different alloys are involved such as AZ91D[35],

AZ91E, AZ91E-0.1Ce and AZ91E-0.1Ti[36], AZ91E-0.1Ag, AZ91E-0.5Ag and

AZ91E-2Y[37], ZK61 and AM60[38], AZ80[39], LA83[40], AZ31B[41] and AZ31[42]

alloys.
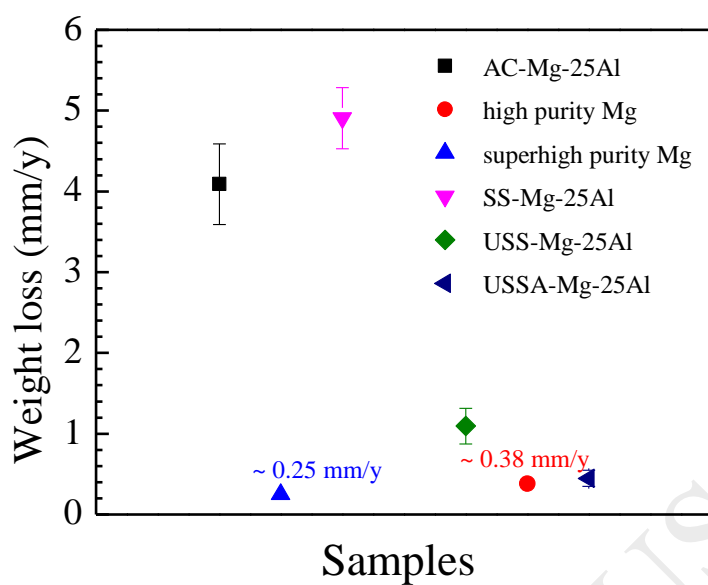
Figure 7. Long-term corrosion properties. (a) Average corrosion rate values based on weight

loss after 6 days immersion in 3.5 wt.% NaCl for different stateMg-25Al alloys. The deviation

was calculated based on three tests. Superhigh purity Mg (~0.25 mm/y [26]) and high purity

Mg (~0.38 mm/y [5]).
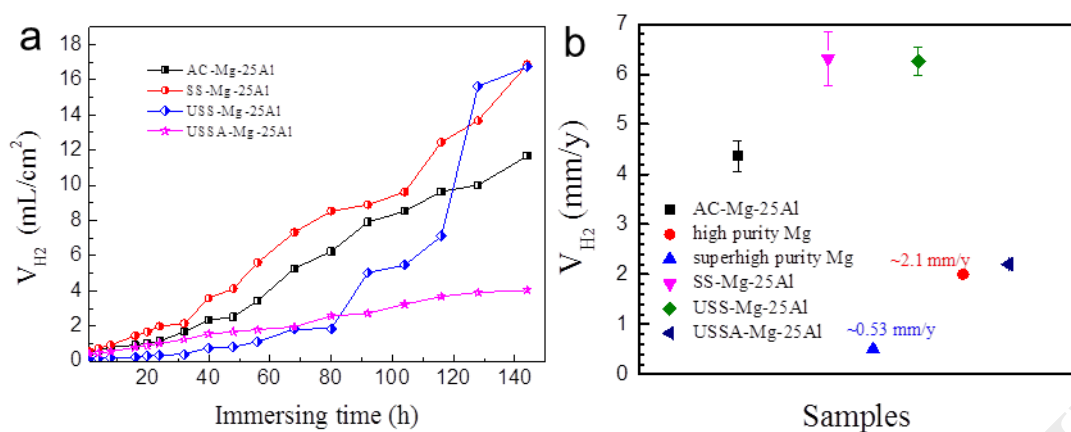
Figure 8. (a) Volume of hydrogen release and (b) the average corrosion rates based on three

samples. Superhigh purity Mg (~0.53 mm/y [26]) and high purity Mg (~2.10 mm/y [5, 44]).
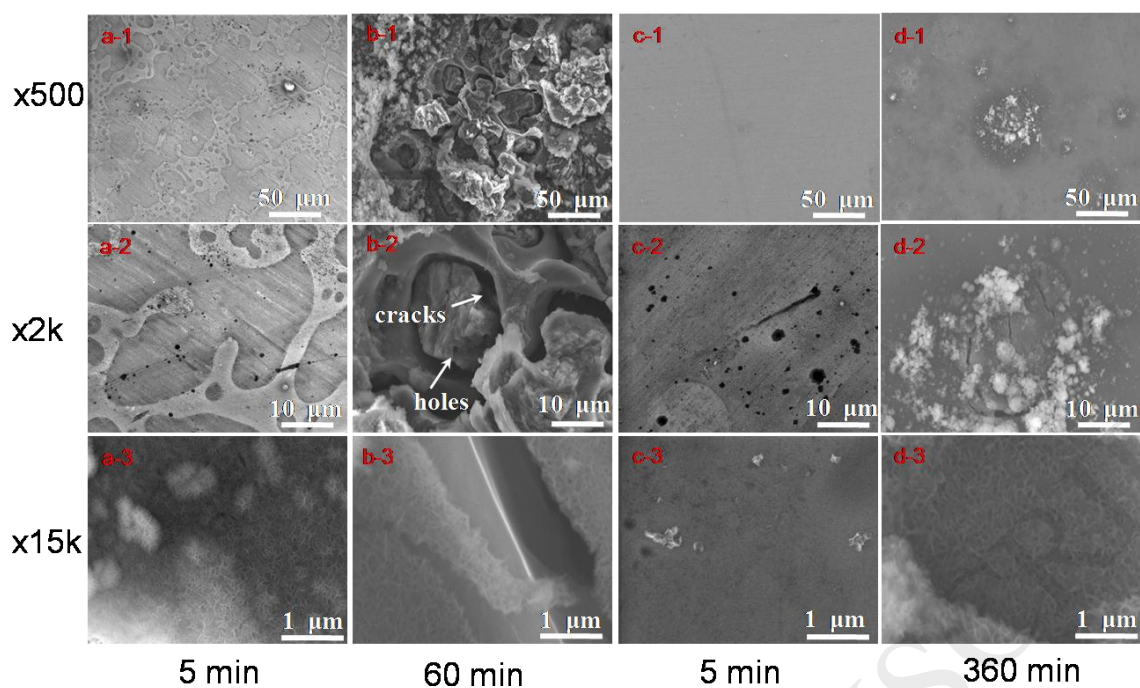
Figure 9. The initiation and expansion of corrosion products. The testing has been carried out

in 3.5 wt.% NaCl solution for different immersing times: AC-Mg-25Al immersing for 5 min (a)

and 60 min (b); USSA-Mg-25Al immersing for 5 min (c) and 360 min (d).
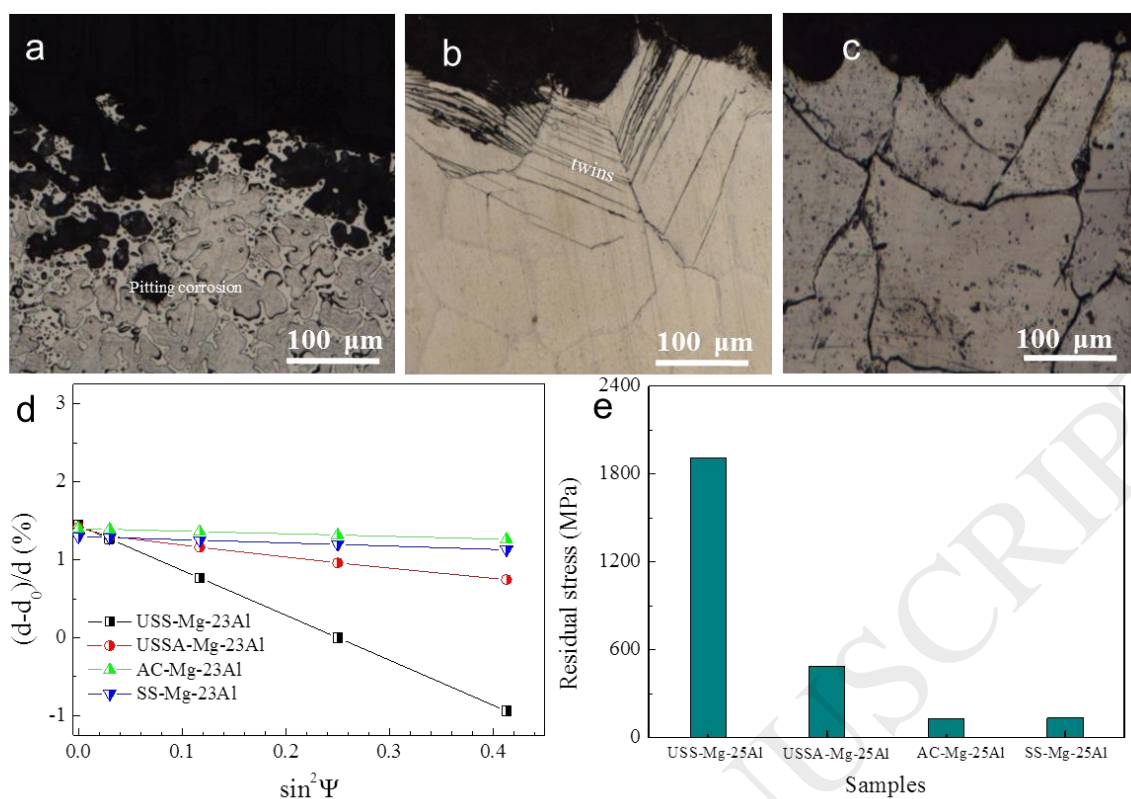
Figure 10. Mechanisms of corrosion resistance. (a), (b) and (c) are related to cross-section

microstructures of SS-Mg-25Al, USS-Mg-25Al and USSA-Mg-25Al after immersed in 3.5

wt.%NaCl for 360 min, respectively. A twin band with a width of 150-200 nm is observed

near to the surface of oxide layer for the USS-Mg-25Al sample. (d) The fitting relationship

between plane spacing and ψ. (e) Residual stress of different state Mg-25Al alloys in terms of

XRD patterns.
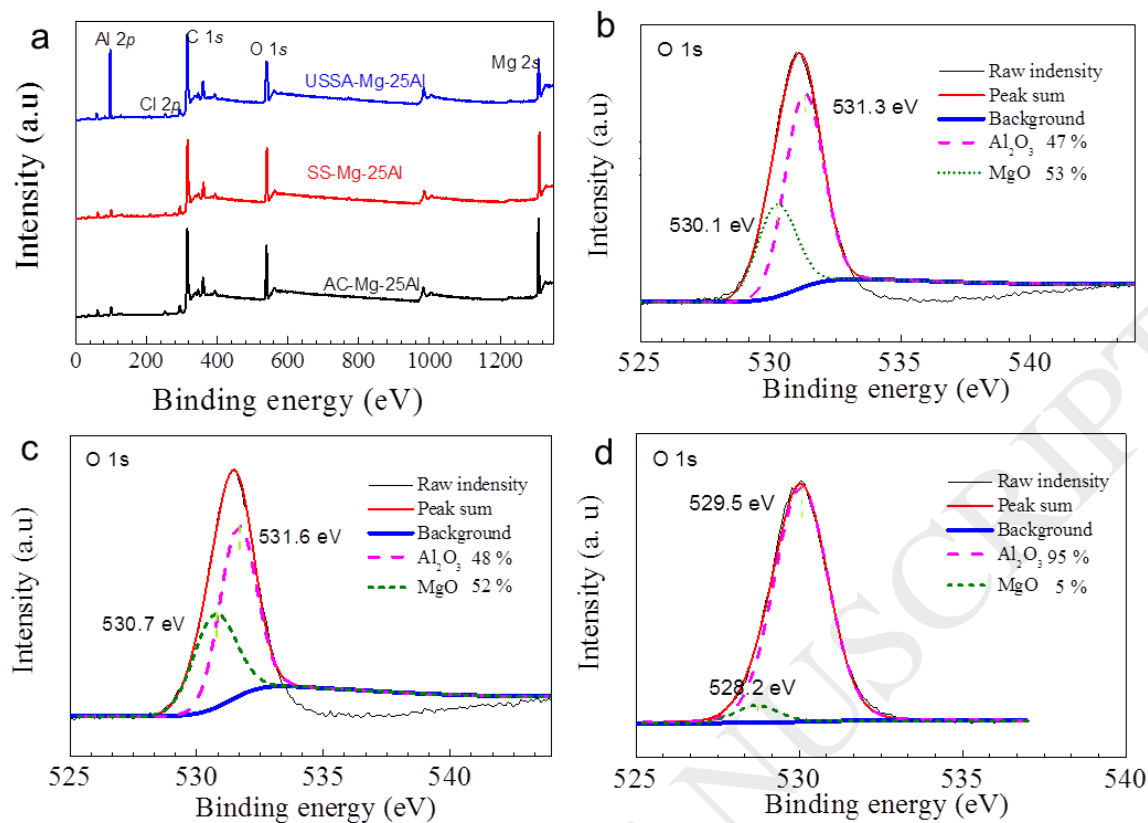
Figure 11. (a) XPS spectra of the different state Mg-25Al alloys after immersed in

3.5wt.%NaCl for 360 min. The fitting chemical compositions of oxides in AC-Mg-25Al (b),

SS-Mg-25Al (c) and USSA-Mg-25Al (d), respectively.